Final Draft

of the original manuscript

Wang, J.; Jin, C.; Mei, D.; Ding, Y.; Chang, L.; Zhu, S.; Wang, L.; Feng, Y.; Guan, S.:

Synthesis and degradation behaviour of Zn-modified coating on Mg alloy.

In: Surface Engineering. Vol. 37 (2021) 8, 963 - 971.

First published online by Maney Publishing: 16.11.2020

https://dx.doi.org/10.1080/02670844.2020.1840827

Synthesis and degradation behaviour of Zn-modified coating on Mg alloy

Jun Wang[a, b, c], Chaoyang Jin[a], Di Mei[a, d], Yan Ding[a], Lei Chang[a, b, c], Shijie Zhu[a, b, c], Liguo Wang[a, b, c *], Yashan Feng[a], Shaokang Guan[a, b, c *]

[a]*School of Material Science and Engineering, Zhengzhou University, Zhengzhou，450001, China*

[b]*Henan Key Laboratory of Advanced Magnesium Alloys, Zhengzhou 450002, China*

[c]*Key Laboratory of Advanced Materials Processing & Mold, Ministry of Education, Zhengzhou 450002, China*

[d]*Magnesium Innovation Centre - MagIC, Institute of Materials Research, Helmholtz-Zentrum Geesthacht, Geesthacht, 21502, Germany*

[*]Corresponding Author:

E-mail address: lgwang@zzu.edu.cn

E-mail address: skguan@zzu.edu.cn

Synthesis and degradation behaviour of Zn-modified coating on Mg alloy

ABSTRACT:

This study aimed to control the degradation of Mg-Zn-Ca alloy and improve its biocompatibility using a biodegradable Zn-modified calcium phosphate coating via dual-pulse electrodeposition. The formation mode and process of the coating were studied herein. Scanning electron microscopy revealed that the coating particles were compactly and neatly packed, and X-ray diffraction analysis, transmission electron microscopy, Fourier transform infrared spectrophotometer and X-ray photoelectron spectroscopy revealed that the coating comprises $CaZn_2(PO_4)_2 \bullet 2H_2O$. The introduction of Zn changes the formation mechanism of coating. The degradation behaviour of the coated Mg alloy was investigated via immersion test and electrochemical test in simulated body fluid. The results show that this non-stoichiometric Zn-modified calcium phosphate coating is biodegradable and has a better protective effect. In addition, the Zn-containing coating has hydrophilic property which is beneficial to enhance the cellular response to the implant's surface and increase apatite formation rate.

KEYWORDS: Mg alloy; Zn-modified calcium phosphate; Coating; Formation mechanism; Degradation behaviour.

1 Introduction

Mg is potentially applicable as a material for biodegradable implants because of its biocompatibility and suitable mechanical properties [1, 2]. However, the intrinsic high corrosion rate of magnesium alloys restricts their biomedical applications [3, 4]. Given the high chemical activity of Mg, magnesium alloys are easy to be corroded and would cause cell death owing to the high concentration of released Mg^{2+} [5]. The modifications by surface engineering lead to improved properties such as corrosion resistance and mechanical properties [4, 6]. In recent years, calcium phosphate coatings have been used to improve the biocompatibility and corrosion resistance of magnesium alloys [7-10]. Moreover, numerous studies have focused on element-modified calcium phosphate coatings, including fluorinated hydroxyapatite (fluorine-dope) [11, 12] and strontium-substituted hydroxyapatite (strontium-dope) [13, 14], since these doped elements can promote fracture healing.

Zn has been found as a beneficial element for the healing of fractures, along with strontium and fluorine [15-17]. Zn exerts important effects on the preservation of bone mass by stimulating osteoblastic bone formation and inhibiting osteoclastic bone resorption. Zn deficiency may cause skeletal growth retardation, prolonged bone recovery [18, 19, 20]. However, few studies have focused on Zn-modified calcium phosphate coatings on magnesium substrates. Zn-modified calcium phosphate coatings have been fabricated on niobium, titanium and pure iron substrates via phosphation [21, 22], plasma electrolytic oxidation [23], and pulsed electro-deposition [24]. The bioactivity of Zn-modified calcium phosphate coatings on pure iron and titanium have been previously proven [21, 23, 24]. Furko et al. [20] have reported that pulse electrodeposited Zn substituted HAp on Ti6Al4V can improve corrosion resistance and enhances biological properties. However, since the dual inhibition effect of Mg^{2+} and

Zn^{2+} on the crystallization of calcium phosphate, Zn-modified calcium phosphate coating is not easy to be fabricated on Mg alloy. Zeng [25] et al. have tried to fabricate Zn-Ca phosphate coating on Mg-Li-Ca substrates via phosphation. However, the morphology of obtained coating is ununiform and incompact, which restricts the performance of the coating. Dual-pulse electrodeposition has been regarded as an effective approach to fabricate the uniform Ca-P coating on Mg alloy [8]. Thus, it is worthy for fabricating the Zn-modified calcium phosphate on Mg alloys via electrodeposition which is probably beneficial for obtaining a compact and uniform coating.

In this study, Zn-modified calcium phosphate coating was successfully produced on Mg-Zn-Ca alloy via dual-pulse electrodeposition to control its degradation. The formation mode and process of this coating ware discussed. The degradation behaviour of coated Mg-Zn-Ca and wettability were also investigated. This study expands the coating technology of biomedical Mg alloys and is beneficial for their application.

2 Materials and methods

2.1 Specimen preparation

The Mg-2.2wt%Zn-0.22wt%Ca alloy was cut into pieces of 25×10×4 mm^3. Before electrodeposition, samples were polished using silicon carbide papers of 100-1000 grits to ensure uniform surface roughness and then cleaned ultrasonically in an alcohol/acetone mixture for 10 min to eliminate residual grease, followed by drying with a blower.

2.2 Coating preparation

Electrolytes for the Zn-containing coating were prepared by a mixing a solution of 0.04 mol/L $Ca(NO_3)_2•2H_2O$, 0.002mol/L $Zn(NO_3)_2•2H_2O$, 0.025 mol/L $NH_4H_2PO_4$, and 0.1 mol/L $NaNO_3$. The electrical parameters were the same as those used in a previous

study [8]. Deposition of Zn-containing coating was carried out at 80°C for 20, 30, 40, 50, and 60min, respectively. Thereafter, the specimens were rinsed in distilled water and air-dried. Zn-free coating deposited for 40 and 50min was employed as a control.

2.3 Microstructure characterization and composition analysis

The surface morphology and element composition of the coatings were assessed using a scanning electron microscope (SEM, Quanta-200) equipped with an energy dispersion spectroscopy (EDS) system. Structural analysis of the coating was carried out using an X-ray diffractometer (XRD, Riguka Ultima IV) with Cu Kα radiations at a scan rate of 4°/min in the 2θ range of 5-80°. In order to further analyse the phase structure of the coating, the coating on Mg alloy was gently scraped off, and was dispersed in absolute alcohol by ultrasonic wave, then the solution was dripped onto the copper mesh and dried out. The transmission electron microscopy (TEM) images were acquired using transmission electron microscope (TEM, JEOL JEM-2100). Chemical compositions of coating were also revealed via Fourier transform infrared spectrophotometer (FT-IR, Thermo Fisher Scientific Nicolet 6700) in the regular wave-numbers range (600-3800 cm^{-1}) and X-ray photoelectron spectroscopy (XPS, Thermo Fisher ESCALAB 250X) with an Al Kα X-ray source. The thickness of coating was measured by eddy current thickness meter (Fisher Dualscope MP0).

2.4 Electrochemical analysis

Dynamic polarization and electrochemical impedance spectroscopy (EIS) were used to study the corrosion behaviour of the coatings. EIS test was performed in the frequency ranges of 100 kHz-10 mHz. The counter electrode was composed of platinum and the reference electrode was a saturated calomel electrode. The area of the working electrode exposed to the solution was 1 cm^2. The measurements were carried out at a scan rate of 0.5 mV/s. Samples were immersed in simulated body fluid (SBF) for 1h to establish a

relatively stable open circuit potential before the study. The corrosion current density (i_{corr}) and corrosion potential (E_{corr}) were obtained through Tafel extrapolation method. The i_{corr} ($A \cdot cm^{-2}$) was converted to degradation rate, P_i ($mm \cdot year^{-1}$), using the following formula [26]:

$$P_i = 0.02285 i_{corr} \quad (1)$$

2.5 Immersion test

Immersion tests were carried out in SBF solution at 36.5 ± 0.5°C for 1 d, 3 d and 7 d. Before immersion, all samples were carefully embedded in the epoxy resin with only one side of 1 cm^2 exposed. Thereafter, the samples were immersed in 20mL SBF solution in a sterilized bottle. The corrosive medium was changed every 24h. After the immersion tests, the samples were cleaned with distilled water and examined via SEM/EDS.

2.6 Water contact angles test

Water contact angles with 5 mL drops of ultrapure water were measured by a contact angle meter (JGW-360a), and the average values were calculated by testing at least three different positions of each sample.

3 Results and discussion

3.1 Morphology of coatings on Mg alloy

The microtopography of the Zn-containing coating (a, b, c, d, e, f, g) and Zn-free coating (h, i) in different deposited periods are presented in Fig. 1. As shown in Fig. 1(a), at a reaction period of 20 min, the crystal clusters with flower-like shape are distributed on the surface of substrates. With the increase of processing time, nucleation of new small crystals and the growth of the original crystal continuously decrease the bare area of substrates, as shown in Fig. 1(b-c). Owing to the supersaturation of phosphates in the electrolyte near the magnesium substrate, the coating gradually

covered the surface. As shown in Fig. 1(d), at a reaction time of 50min, the substrate is completely covered. Fig. 1(e) shows the morphology of the sample generated for 50min at a higher magnification, and the joint is clearly visible because the adjacent clusters grow and interact with one another. Because of the continuous effects of external forces, hydrogen produced through hydrogen evolution damages the coating after the coating completely envelopes the surface, and pores appear on the coating with an increase of processing time, as shown in Fig. 1(f, g). Afterwards, the pores are covered by new crystals again, and new pores are simultaneously formed. Thus, the aforementioned results indicate that the coating generated for 50 min has the best morphology.

3.2 Chemical composition, phase structure and thickness of coatings on Mg alloy

The chemical compositions of the areas J-O in Fig.1 (a, d, g, h) analysed via EDS are shown in Table 1. On comparing between areas J and K, Mg is detected in the new small crystals (area K) but not in the grown crystals (area J). That is, Mg^{2+}, Ca^{2+} and Zn^{2+} participate in crystal nucleation; only Ca^{2+} and Zn^{2+} participate in crystal growth. Furthermore, only a small amount of Mg^{2+} is produced during electrodeposition, indicating that corrosion of substrates is suppressed during dual-pulse electrodeposition. In the contrast, during phosphation, substrates are continuously corroded by phosphating solution, thus deteriorating the morphology of the Zn-Ca phosphate conversion coating on Mg substrate [25]. Moreover, elemental Mg was detected in undamaged coating (area M). Our results show that the coating generated for 50min has a certain thickness and the molar ratios of Zn/Ca and (Zn+Ca)/P are approximately 2.08 and 1.42, respectively. Since N is the area around the pores and elemental Mg is again detected in this region indicating that the pores can damage the coating and expose the substrate, and the protection capacity of the coating for the substrate correspondingly weakens.

Fig. 2 shows the XRD pattern of the coated Mg alloy. With the addition of Zn, the Zn ions can change the crystal structure of calcium phosphate. Clearly, in spite of substrate peaks, $CaZn_2(PO_4)_2 \cdot 2H_2O$ (PDF No. 35-495) peaks were detected in curve of Zn-containing coating, which demonstrated the successful incorporation of Zn into the calcium phosphate phase. The molar ratios of Zn/Ca in the chemical formula are similar with those determined via EDS; but the ration of (Zn+Ca)/P of coating is little bit lower than that from chemical formula. The mineralogical name of $CaZn_2(PO_4)_2 \cdot 2H_2O$ is parascholzite [27-29]. It is referred to as Zn-modified calcium phosphate in this study sometimes. Fig. 3 (a) shows bright-field TEM image of powers scraped from the coating of Mg alloy. The corresponding selected area electron diffraction (SAED) pattern reveals that the phase of coating is mainly $CaZn_2(PO_4)_2 \cdot 2H_2O$, as shown in Fig. 3(b), (c).

Fig. 4 (a) shows the FTIR spectra of the coatings with and without Zn. The infrared absorption peaks at wavelengths of between 900 and 1200cm^{-1} are attributed to PO_4^{3-} stretching vibration; the absorption peaks of 1630cm^{-1} and between 3100 and 3500cm^{-1} are due to the presence of OH^-; the absorption at 1450cm^{-1} due to the presence of CO_3^{2-}. For Zn-free coating (as shown in Fig.4 (a) A), absorbance peak at about 1388cm^{-1} is due to the P-OH stretching vibration of HPO_4^{2-}, which was not found in Zn-containing coating. From Fig.4, we can see that the infrared absorption peaks of PO_4^{3-} are different for the coatings with and without Zn. The absorption peak of PO_4^{3-} of Zn-free coating is single. However, the absorption peak of PO_4^{3-} becomes a continuous multi-peak when Zn is added in coating. This could be due to the PO_4^{3-} only interacts with Ca^{2+} in Zn-free coating, while the PO_4^{3-} interacts with Ca^{2+} and Zn^{2+} in Zn-containing coating. The different cations affect the energy of P-O stretching vibration.

The thickness is a critical property of coating. A coating that is too thin cannot provide sufficient protection for the substrates, while the coating that is too thick has low adhesive strength and easy to partly detach from the substrate. In this study, the thickness of the Zn-containing coating is 8.38 μm. Xia et al. [30] have investigated the critical cracking thickness of biomimetic CaPs coating, which is 2 μm. However, the critical thickness in different coating system may not constant. In our case, we believe that there are a number of factors effecting the critical cracking thickness, such as substrate surface state, morphology and particle sizes of calcium phosphates, the formation mode of the coating etc. More investigations will be performed in the future to verify the critical thickness for crack formation in this coating system.

3.3 Coating formation mechanism

Fig.5 shows a schematic diagram of the Zn-containing coating formation mechanism. In the first step, when the magnesium alloy substrate is immersed in the electrolyte solution, the surface will naturally occur slight corrosion, Mg^{2+} will be dissolved and hydrogen bubbles will appear on the surface of Mg substrate, as shown in Fig.5(a). In the second step, the hydrogen evolution reaction occurs on the surface of the Mg substrate under a positive voltage. Hydrogen ions involved in the reaction are derived from $H_2PO_4^-$ and HPO_4^{2-}. Mg is dissolved during hydrogen evolution at a negative voltage, as shown in Fig.5(b). In the third step, the pH value of electrolytes near the Mg substrate increased because of hydrogen evolution, as described by the Eq. 2 and Eq. 3 [31].

$$2H_2O + 2e^- \rightarrow H_2\uparrow + 2OH^- \quad (2)$$

$$Mg \rightarrow Mg^{2+} + 2e^- \quad (3)$$

Thereafter, the increase of pH value decreased the solubility for certain types of phosphates, e.g. those of Zn^{2+}, Ca^{2+}, and PO_4^{3-}. Phosphate crystals separate out and are

deposited on the substrate. The crystal clusters were distributed on the surface (Fig. 5[c]). then, nucleation of new small crystals and the growth of the original crystal continuously decreases the bare area of substrates (Fig. 5[d]). In the fourth step, owing to the supersaturation of phosphates in the electrolyte near the Mg substrate, the coating gradually covered the surface (Fig. 5[e]). In the fifth step, because of the effects of external voltage, the continuous evolved hydrogen (as shown in Eq.3) damages the coating after the coating completely envelopes the surface, and then pores appear on the coating with an increase of processing time (Fig. 5[f]).

3.4 Degradation behavior and hydrophilicity

The degradation behavior of coating is critical for Mg alloys as temporary implant materials. Degradation morphologies of the coated Mg-Zn-Ca after immersion test in SBF for 1 d, 3 d and 7 d are shown in Fig. 6 (a-c) and the chemical compositions of the areas in Fig.6 (a-c) determined via energy dispersion spectroscopy are shown in Table 2. The results showed that the coating was not damaged after 1 d and 3 d of immersion, and the chemical compositions of the coating remained unchanged (as shown in areas D and E). When the immersion time was extended to 7 d, many parts of the coating remained unchanged (as shown in area F); however, a part of the coating was disrupted (as shown in area H) and degradation products started accumulating around these sites (as shown in area G). Moreover, both areas G and H are characterized by a high amount of elemental Mg and a relatively low elemental Zn concentration, implying that degradation products of Mg alloy were predominant at these sites. It could be concluded that the coating eventually degrades during immersion.

The potentiodynamic data were analysed to obtain the electrochemical parameters and the results were shown in Fig.7 and Table 3. As it can be seen from Fig. 7 and Table 3, the corrosion potential of the Mg alloy with Zn-modified coating increased to -

1.66V, and the corrosion current density decreased by approximately two-fold in comparison with that of the bare Mg-alloy and by approximately one-fold in comparison with that of the normal calcium phosphate coating. The Mg alloys without coating possesses the highest corrosion current ($i_{corr.}$) in the SBF, while the lowest corrosion rate and highest corrosion resistance belongs to Zn-modified calcium phosphate coatings. The results of the EIS test (Fig. 7b) showed the obvious different EIS plots for samples with different coatings. For the sample with Zn-containing coating, the diameter of the capacitive arc was much larger than that of the sample with Zn-free coating, indicating improved corrosion resistance. The results of the EIS test are consistent with the results of polarisation curves. Our results show that the Zn-modified coating can significantly improve the substrate corrosion resistance and displays better protective effects than the normal calcium phosphate coating.

For the coating on biodegradable metallic materials, the biodegradability and corrosion resistance seem two contradictory properties. Generally, the inorganic calcium phosphate coatings should not have sufficient biodegradability since their low solubility. But in this study, the parascholzite coating fabricated by dual-pulse electrodeposition shows biodegradability. As we mentioned in the text, the ratio of (Zn+Ca)/P of coating (1.42) is little bit lower than the nominal value (1.50) from chemical formula. Compared with normal inorganic coating, the non-stoichiometric coating has been proven to have good biodegradability [8]. This allows the coating to retard the corrosion of the substrate without altering its degradable properties.

The normal calcium phosphate coatings on magnesium have needle-like or rod-like features, the gap between different crystal is the approach for corrosive media to reach the substrate, which is harmful for the corrosion resistance. The incorporation of Zn alters the formation mode of the coating, the compactly and neatly packed crystals are

found in Zn-containing coating. The compact Zn-containing coating provides more protection to the substrate and acts as barrier against the corrosive attack of the corrosive liquid. Prado reported that [22] Zn incorporation to the solution decreased nucleation and growth, which was associated to the lower affinity of Zn with oxygen when compared with calcium, due to the lower Zn electronegativity difference, which increased the energy barrier for nucleation. According to the morphology of coating in this study, the Zn incorporation to the solution decreased nucleation, while growth rate increased, thus it takes even longer time for the substrate being completely covered by coating.

Fig. 7 (c-e) exhibits the contact angles of the bare Mg alloys, Zn-free and Zn-containing coating samples. The contact angle of the bare Mg alloys is 88.07° , and with coatings, the contact angle was decreased. The coatings demonstrated favorable hydrophilic property and Zn-containing coating exhibited the lowest contact angle amongst them, which is mainly because of the changes of surface morphology and structure. The Zn-free coating has needle-like or rod-like features with nano-scale, which is of no advantage to interact with water; while Zn-containing coating is bloom shape with micro-scale, which is more effective to improve wettability. Sub-sequent to the implantation, the absorption of proteins starts at the surface of implants from extracellular matrix. Hydrophilic surfaces increase the adsorption of cell adhesion- promoting proteins on their surfaces [32-34]. Such increased adsorption of extracellular matrix proteins increases early bone apposition [35]. In addition, rapid apatite formation was achieved on highly hydrophilic surfaces [35]. Reportedly, hydrophilic nature enhances the cellular response to the implant's surface and increases apatite formation rate.

4 Conclusions

In the present study, a novel biodegradable coating of Zn-modified calcium phosphate was successfully deposited on a Mg-Zn-Ca alloy. The coating comprises $CaZn_2(PO_4)_2 \cdot 2H_2O$. The introduction of Zn changes the formation mechanism of coating. The immersion test indicated that the coating degrades gradually during immersion. Electrochemical analysis revealed that the Zn-modified calcium phosphate coating improves the corrosion resistance of the Mg-Zn-Ca alloy and has a better protective effect than the normal calcium phosphate coating. Furthermore, the Zn-containing coating has hydrophilic property which is beneficial to enhance the cellular response to the implant's surface and increases apatite formation rate, which open a new window for improving the corrosion resistance of bio-Mg alloys, especially for orthopedic implantation application.

In summary, the Zn-containing coating could be a promising strategy to enhance the surface properties, corrosion resistance and wettability of Mg alloys implants and thus it deserves further biological evaluation to ascertain their usefulness for clinical applications. The forthcoming stage of research will be focused on the potential antibacterial activity, biocompatibility and bone healing ability of coating to provide a comprehensive understanding of Zn-containing coating.

Acknowledgements

This work was supported by the Key Projects of the Joint Fund of the National Natural Science Foundation of China (U1804251), National Natural Science Foundation of China (51701184, 51671175, 51601169), National Key Research and Development Program of China (2018YFC1106703), and Henan Key Scientific Research Project (16A430029).

Disclosure statement

No potential conflict of interest was reported by the authors.

References

[1] Zheng YF, Gu XN, Witte F. Biodegradable metals. Mat Sci Eng R. 2014; **77**: 1-34.

[2] Zou YH, Wang J, Cui LY, et al. Corrosion resistance and antibacterial activity of zinc-loaded montmorillonite coatings on biodegradable magnesium alloy AZ31. Acta Biomater. 2019; 98: 196-214.

[3] Guan XR, Zhu HD, Shi JW, et al. Influence of zinc-dipping on electroless nickel coating on magnesium alloy. Surf Eng. 2019; 35: 906-912.

[4] Roshan NR, Hassannejad H, Nouri A. Corrosion and mechanical behaviour of biodegradable PLA-cellulose nanocomposite coating on AZ31 magnesium alloy. Surf Eng. 2020; doi: 10.1080/02670844.2020.1776093.

[5] Song XZ, Chang L, Wang J, et al. Investigation on the in vitro cytocompatibility of Mg-Zn-Y-Nd-Zr alloys as degradable orthopaedic implant materials. J. Mater. Sci. Mater Med. 2018; 29: 44.

[6] Constantino ME, Campillo B, Staia MH, et al. Pulsed electrode deposition of superhard coatings on steel substrates: microstructural and chemical study. Surf Eng. 2006; 22 (3): 212-218.

[7] Ji XJ, Cheng Q, Wang J, et al. Corrosion resistance and antibacterial effects of hydroxyapatite coating induced by polyacrylic acid and gentamicin sulfate on magnesium alloy. Front Mater Sci. 2019; 13(1): 87-98.

[8] Wang HX, Guan SK, Wang X, et al. In vitro degradation and mechanical integrity of Mg-Zn-Ca alloy coated with Ca-deficient hydroxyapatite by the pulse electrodeposition process. Acta Biomater. 2010; 6: 1743-1748.

[9] Saadati A, Hesarikia H, Nourani MR, et al. Electrophoretic deposition of hydroxyapatite coating on biodegradable Mg-4Zn-4Sn-0.6Ca-0.5Mn alloy. Surf Eng. 2019; doi: 10.1080/02670844.2019.1661145.

[10] Fan XL, Li CY, Wang YB, et al. Corrosion resistance of an amino acid-bioinspired calcium phosphate coating on magnesium alloy AZ31. J Mater Sci Technol. 2020; 49: 224-235.

[11] Wang Y, Li X, Chen M, et al. In Vitro and in Vivo Degradation Behavior and Biocompatibility Evaluation of Microarc Oxidation-Fluoridated Hydroxyapatite-Coated Mg-Zn-Zr-Sr Alloy for Bone Application. ACS Biomater Sci Eng. 2019; 5(6): 2858-2876.

[12] Sonamuthu J, Samayanan S, Jeyaraman AR, et al. Influences of ionic liquid and temperature on the tailorable surface morphology of F-apatite nanocomposites for enhancing biological abilities for orthopedic implantation. Mat Sci Eng C. 2018; 84: 99-107.

[13] Makkar P, Kang HJ, Padalhin AR. In-vitro and in-vivo evaluation of strontium doped calcium phosphate coatings on biodegradable magnesium alloy for bone applications. Appl Surf Sci. 2020; 510:145333

[14] Wang T, Yang G, Zhou W, et al. One-pot hydrothermal synthesis, in vitro biodegradation and biocompatibility of Sr-doped nanorod/nanowire hydroxyapatite coatings on ZK60 magnesium alloy. J Alloy Compd. 2019; 799: 71-82.

[15] Zhang RN, Zhang LL. A functionalised carbon nanotube-gelatin-Zn doped HA composite coating for bone grafting application. Mater Technol. 2020; DOI: 10.1080/10667857.2020.1760508

[16] Wang Z, Wang XY, Tian Y, et al. Degradation and osteogenic induction of a SrHPO4-coated Mg-Nd-Zn-Zr alloy intramedullary nail in a rat femoral shaft fracture model. Biomaterials. 2020; 247: 119962.

[17] Yu JM, Xu LZ, Li K, et al. Zinc-modified Calcium Silicate Coatings Promote Osteogenic Differentiation through TGF-beta/Smad Pathway and Osseointegration in Osteopenic Rabbits. Sci Rep. 2017; 7: 3440.

[18] O'Connor JP, Kanjilal D, Teitelbaum M, et al. Zinc as a Therapeutic Agent in Bone Regeneration. Materials. 2020; 13(10): 2211.

[19] Popa CL, Deniaud A, Michaud-Soret I, et al. Structural and Biological Assessment of Zinc Doped Hydroxyapatite Nanoparticles. J Nanomater. 2016; 2016: 1062878.

[20] Furko M, Jiang YH, Wilkins T, et al. Development and characterization of silver and zinc doped bioceramic layer on metallic implant materials for orthopaedic application. Ceram Int. 2016; 42: 4924-4931.

[21] Chen HY, Zhang EL, Yang K. Microstructure, corrosion properties and bio-compatibility of calcium zinc phosphate coating on pure iron for biomedical application. Mat Sci Eng C. 2014; 34: 201-206.

[22] Prado Da Silva MH, Moura FN, Navarro Da Rocha D, et al. Zinc-modified hydroxyapatite coatings obtained from parascholzite alkali conversion. Surf Coat Tech. 2014; 249: 109-117.

[23] Park MG, Choe HC. Corrosion Behaviors of Zn, Si, and Mn-Doped Hydroxyapatite Coatings Formed on the Ti-6Al-4V Alloy by Plasma Electrolytic Oxidation. J Nanosci Nanotechno. 2020; 20(9): 5618-5624

[24] Chakraborty R, Mandal M, Saha P. Electrochemical stability and bio-mineralization capability of zinc substituted and elemental zinc reinforced calcium phosphate composite coatings synthesized through pulsed electro-deposition. Ceram Int. 2019; 45(17): 22899-22911.

[25] Zeng RC, Sun XX, Song YW, et al. Influence of solution temperature on corrosion resistance of Zn-Ca phosphate conversion coating on biomedical Mg-Li-Ca alloys. T Non Ferr Metal. Soc. 2013; 23: 3293-3299.

[26] Cui LY, Gao SD, Li PP, et al. Corrosion resistance of a self-healing microarc oxidation/polymethyltrimethoxysilane composite coating on magnesium alloy AZ31. Corros Sci. 2017; 118: 84-95.

[27] Afflerbach, S.; Sharma, S.; Trettin, R. Synthesis, reversibility and mechanism of the dehydration of monoclinic CaZn2(PO4)(2)center dot 2H(2)O. J Solid State Chem. 2018; 265: 274-284

[28] Furko M, Jiang YH, Wilkins T, et al. Development and characterization of silver and zinc doped bioceramic layer on metallic implant materials for orthopedic application. Ceram Int, 2016; 42: 4924-4931.

[29] Karacan I, Senturk D, Oktar FN, et al. Structural and characterisation analysis of zinc-substituted hydroxyapatite with wet chemical precipitation method. Int J Nano Biomater. 2016; 6: 188-204.

[30] Xia W, Fu L, Engqvist H. Critical cracking thickness of calcium phosphates biomimetic coating: Verification via a Singh-Tirumkudulu model. Ceram Int, 2017; 43: 15729-15734.

[31] Sun RX, Liu P, Zhang RX, et al. Hydrothermal synthesis of microstructured fluoridated hydroxyapatite coating on magnesium alloy. Surf Eng. 2016; 32: 879-884.

[32] Toffoli A, Parisi L, Tatti R. Thermal-induced hydrophilicity enhancement of titanium dental implant surfaces. J Oral Sci. 2020; 62(2): 217-221.

[33] Eriksson C, Nygren H, Ohlson K. Implantation of hydrophilic and hydrophobic titanium discs in rat tibia: cellular reactions on the surfaces during the first 3 weeks in bone. Biomaterials. 2004; 25: 4759-4766.

[34] Hotchkiss KM, Clark NM, Olivares NR. Macrophage response to hydrophilic biomaterials regulates MSC recruitment and T-helper cell populations. Biomaterials. 2018; 182: 202-215.

[35] Park JW, Kim YJ, Jang JH. Enhanced osteoblast response to hydrophilic strontium and/or phosphate ions-incorporated titanium oxide surfaces. Clin Oral Implan Res. 2010; 21: 398-408.

TABLE 1: Chemical compositions of the areas J-O in Fig.1 (a, d, g, h) determined through energy dispersion spectroscopy

Areas	Elements (at.%)					
	Ca	Zn	Mg	P	O	C
J	8.14	16.33	-	17.71	42.67	15.15
K	6.24	10.40	8.02	12.97	47.61	14.76
L	-	-	81.16	2.87	15.97	-
M	7.30	15.23	-	15.86	45.25	16.36
N	14.66	1.42	8.46	12.49	44.90	18.07
O	19.87	0	-	16.55	46.48	17.10

TABLE 2: Chemical compositions of the areas D-H in Fig.6 (a-c) determined via energy dispersion spectroscopy

Areas	Elements (At%)						
	C	O	Mg	P	Ca	Zn	Na
D	18.92	31.34	2.09	14.69	5.71	11.16	16.09
E	18.73	34.17	1.30	13.65	5.68	11.07	15.40
F	18.43	36.82	1.05	12.72	5.01	9.81	16.15
G	18.03	43.41	7.16	15.12	11.16	1.95	3.19
H	23.54	23.43	36.81	7.91	3.25	2.62	2.44

TABLE 3: Tafel polarization parameters of the tested samples.

Sample	E_{corr} (V)	i_{corr} (A • cm^{-2})	Corrosion rate (mm • y^{-1})
Substrate	-1.7267	1.114E-04	2.545
Zn-containing coating	-1.6618	5.754E-06	0.131
Zn-free coating	-1.6893	3.088E-05	0.687

Figure Captions

Figure 1. Scanning electron micrographs of the Mg alloy with a Zn-containing coating generated for different periods: (a) 20 min, (b) 30 min, (c) 40 min, (d, e) 50 min, and (f, g) 60 min, and Zn-free coating generated for (h) 40min and (i) 50min.

Figure 2. XRD patterns of the coated Mg alloys

Figure 3. TEM and SAED images of the Zn-containing coating: (a) TEM, (b) SAED from the <$\bar{1}$03> direction, (c) SAED from the <103> direction.

Figure 4. Fourier infrared spectroscopy diagrams of the coating without or with Zn: (a) XPS survey spectra of the coated Mg alloys, (b) wide scan, (c) Zn2p; (d) Ca2p, (e) O1s, and (f) P2p.

Figure 5. Schematic diagram of the Zn-containing coating formation mechanism.

Figure 6. Scanning electron micrographs of the coated Mg alloy immersed in simulated body fluid (SBF) for (a) 1 d, (b) 3 d, (c) 7 d.

Figure 7. Potentiodynamic polarization curves (a) and Nyquist plots (b) of samples tested in SBF, and the contact angles of the bare Mg alloys (b), Zn-free coating (c) and Zn-containing coating samples (d).

Figure 1 in TIFF format

Click here to access/download;Non-colour figure;Figure 1.TIF

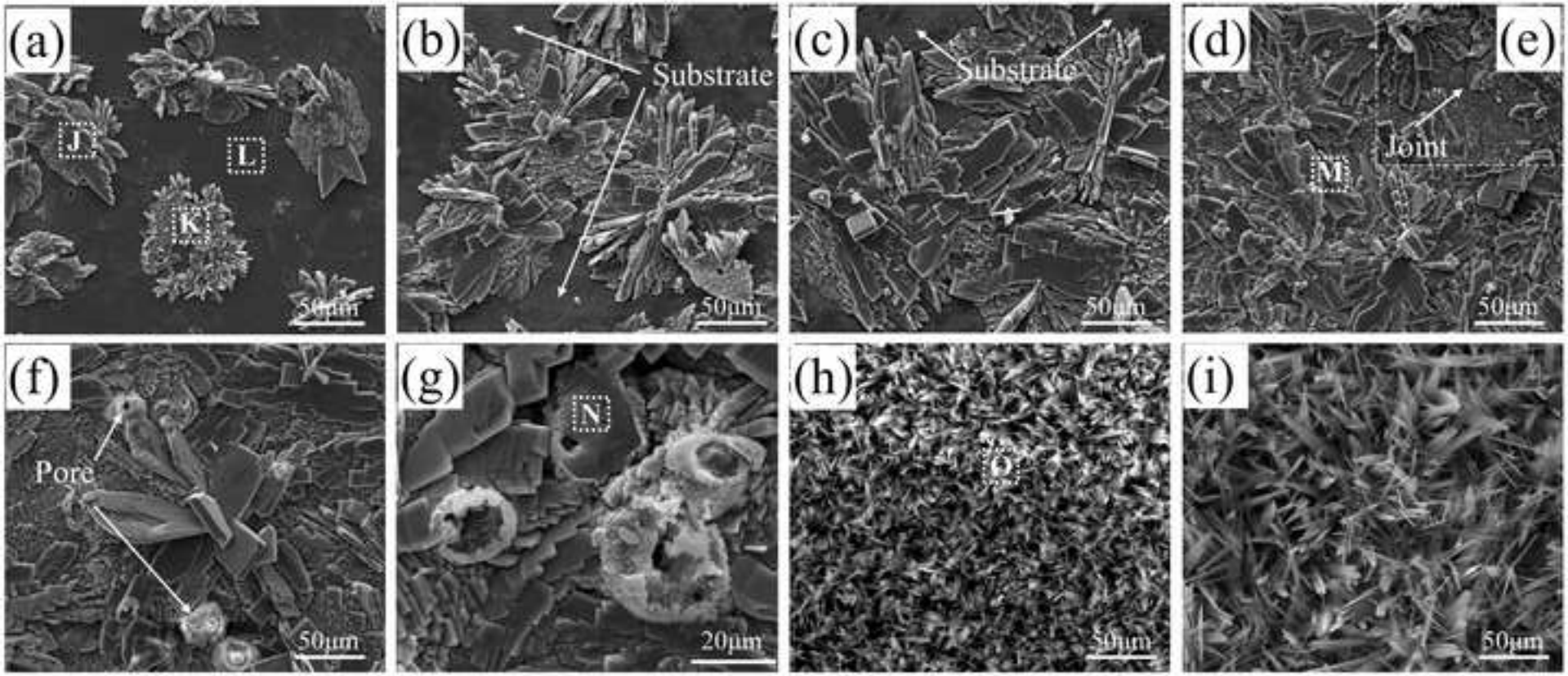

Figure 2 in TIFF format

Click here to access/download;Colour figure (online version only);Figure 2.TIF

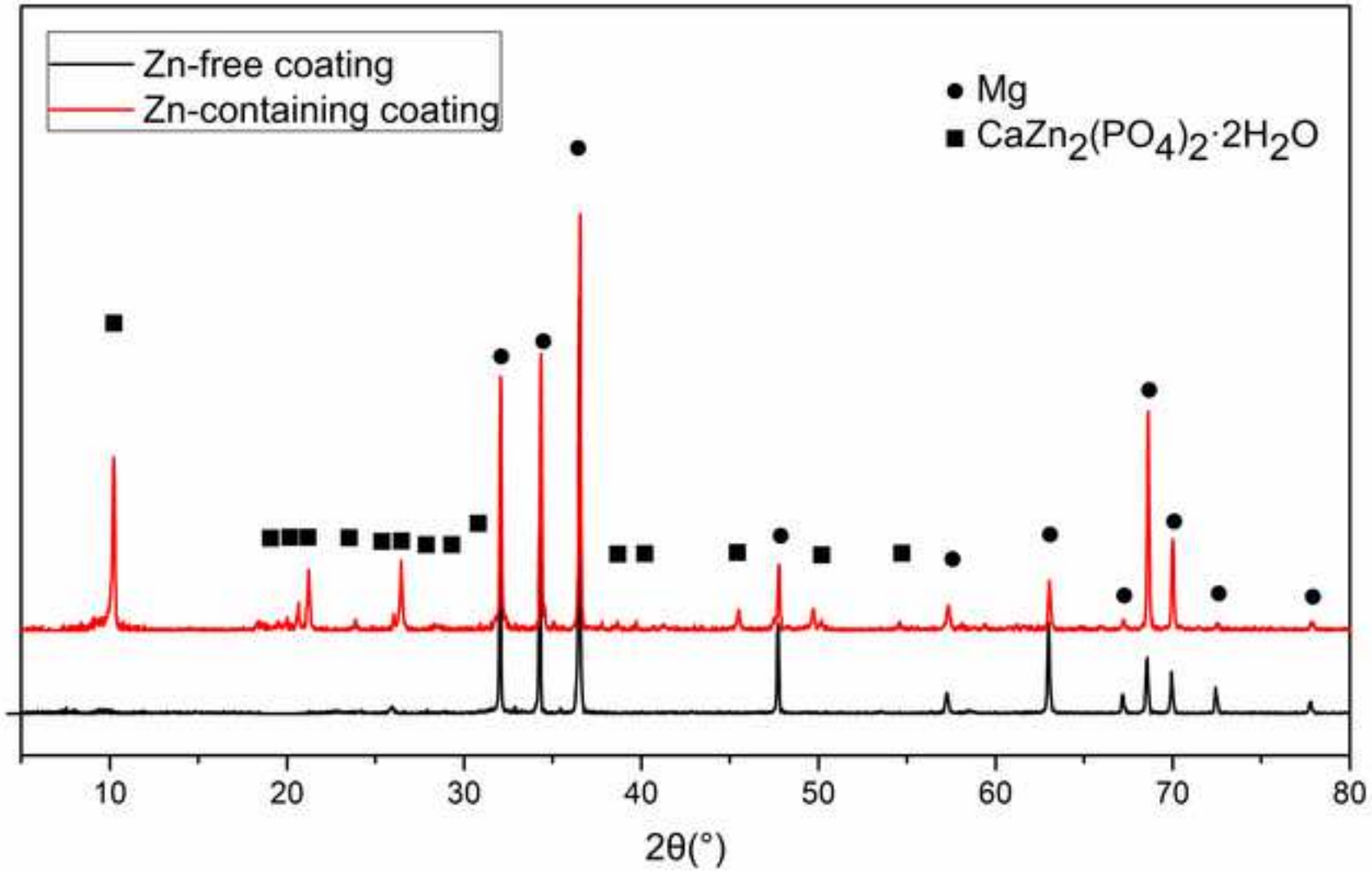

Figure 3 in TIFF format

Click here to access/download;Non-colour figure;Figure 3.TIF

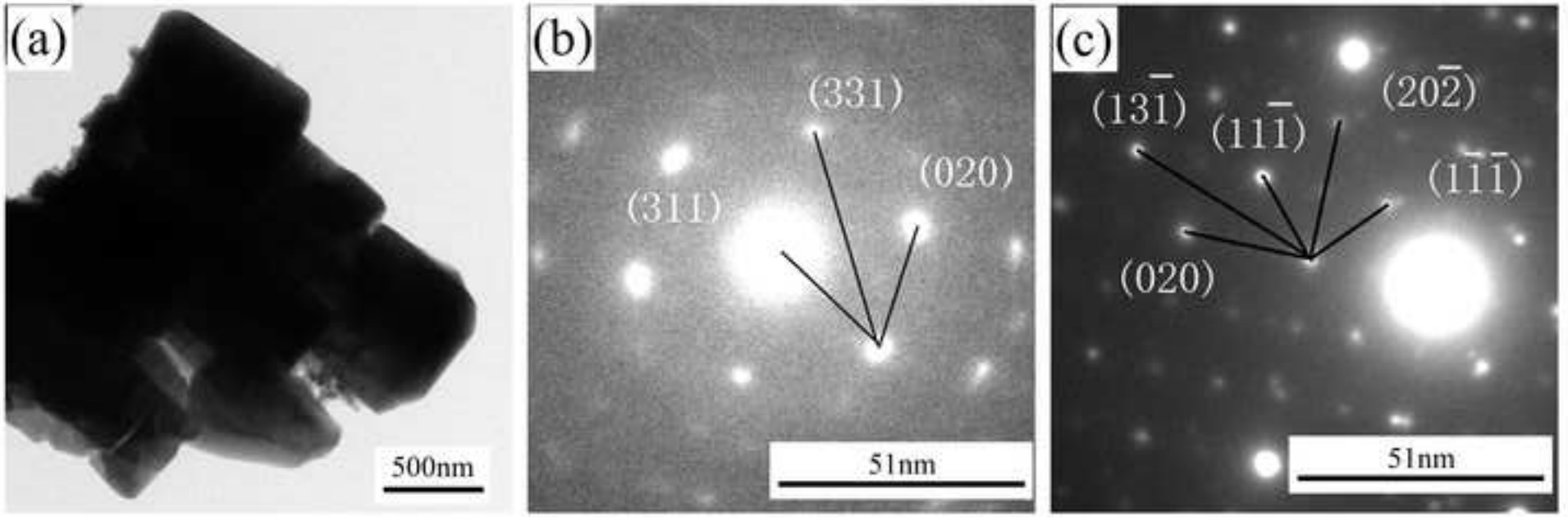

Figure 4 in TIFF format

Click here to access/download;Colour figure (online version only);Figure 4.TIF

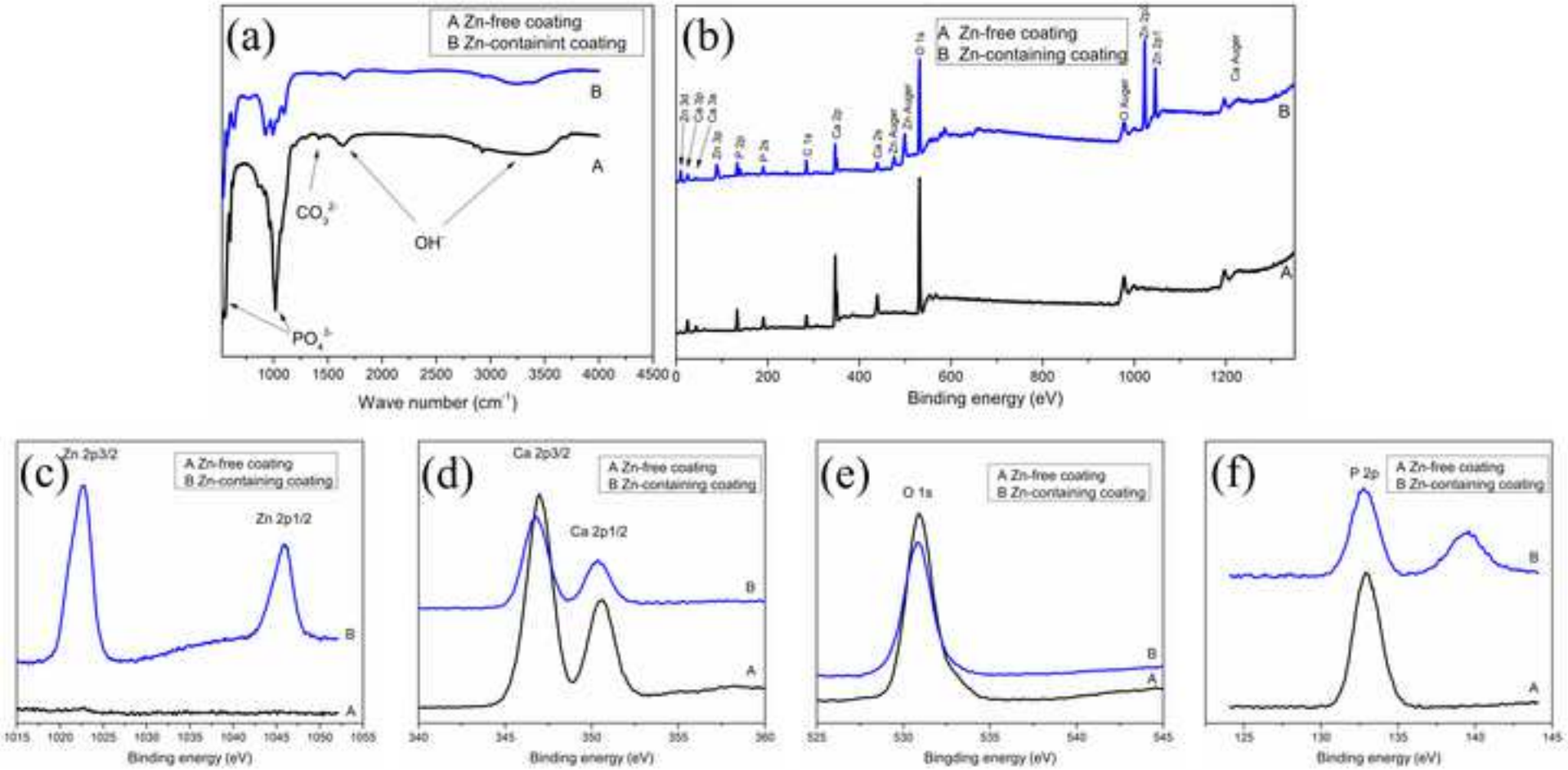

Figure 5 in TIFF format

Click here to access/download;Colour figure (online version only);Figure 5.TIF

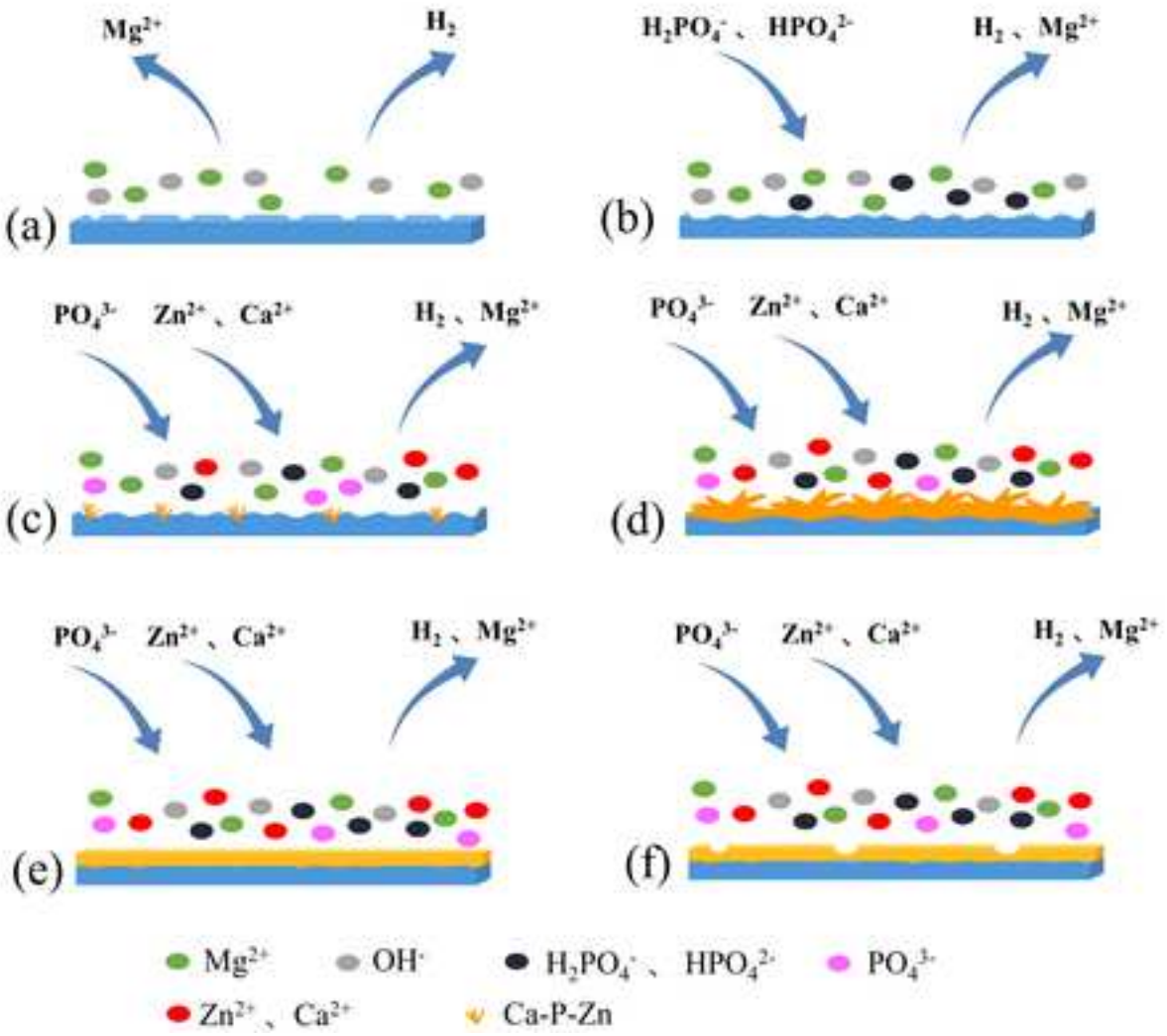

Figure 6 in TIFF format

Click here to access/download;Non-colour figure;Figure 6.TIF

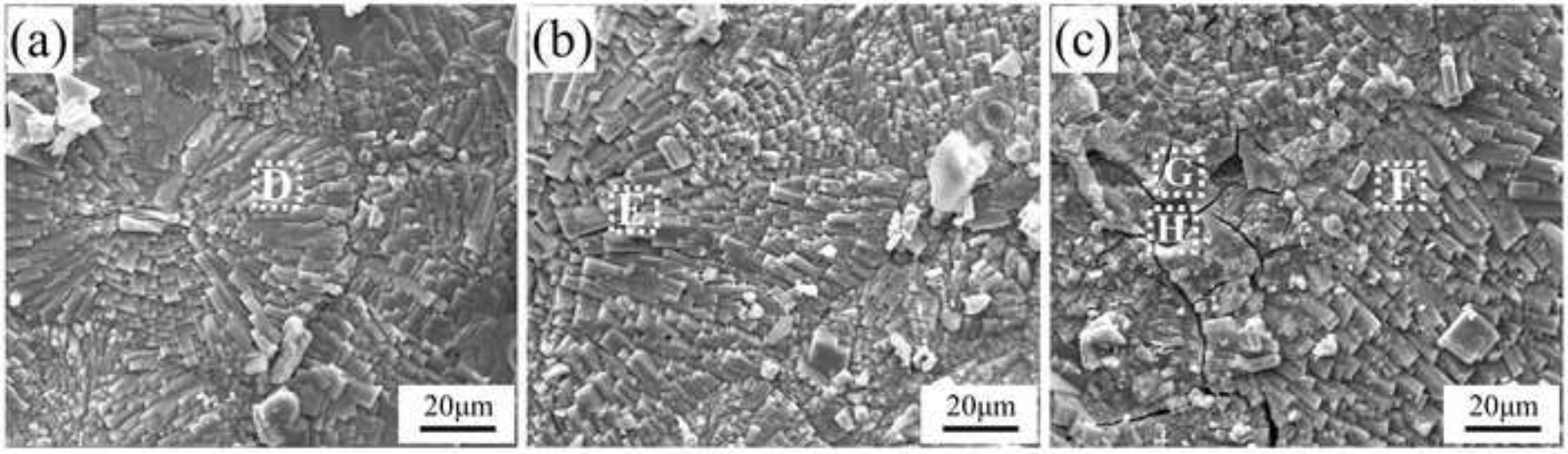

Figure 7 in TIFF format

Click here to access/download;Colour figure (online version only);Figure 7.TIF